Applied Physics Letters

RESEARCH ARTICLE | APRIL 17 2023

Plasma-free dry etching of (001) β-Ga_2O_3 substrates by HCl gas

Takayoshi Oshima ; Yuichi Oshima

Appl. Phys. Lett. 122, 162102 (2023)
https://doi.org/10.1063/5.0138736

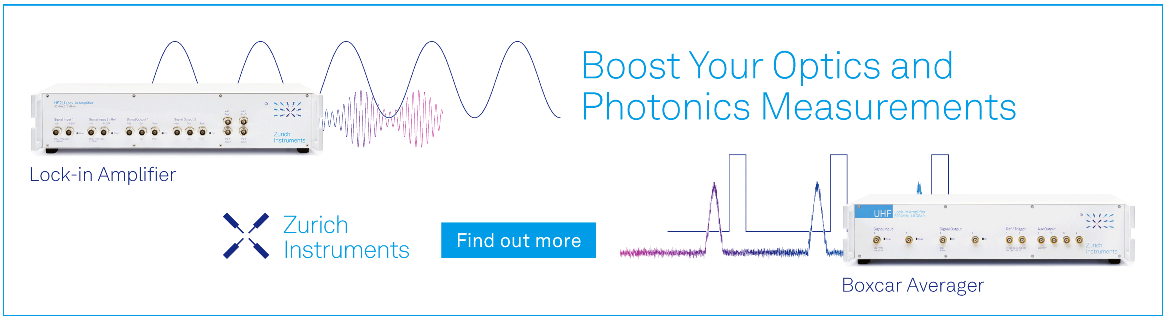

AIP Publishing

Applied Physics Letters ARTICLE scitation.org/journal/apl

Plasma-free dry etching of (001) β-Ga_2O_3 substrates by HCl gas

Cite as: Appl. Phys. Lett. **122**, 162102 (2023); doi: 10.1063/5.0138736
Submitted: 14 December 2022 · Accepted: 5 April 2023 ·
Published Online: 17 April 2023

View Online Export Citation CrossMark

Takayoshi Oshima[a] and Yuichi Oshima

AFFILIATIONS

Research Center for Functional Materials, National Institute for Materials Science, Tsukuba, Ibaraki 305-0044, Japan

[a]Author to whom correspondence should be addressed: OSHIMA.Takayoshi@nims.go.jp

ABSTRACT

In this study, we dry etched SiO_2-masked (001) β-Ga_2O_3 substrates in HCl gas flow at a high temperature without plasma excitation. The etching was done selectively in window areas to form holes or trenches with inner sidewalls of (100) and/or {310} facets, which are the smallest surface-energy-density plane and oxygen-close-packed slip planes, respectively. In particular, (100) faceted sidewalls were flat and relatively close to the substrate surface normal. Therefore, this simple dry etching method is promising for fabricating plasma-damage-free trenches and fins used for β-Ga_2O_3-based power devices.

Monoclinic-structured β-Ga_2O_3 is a promising ultra-wide bandgap semiconductor for power electronics.[1] β-Ga_2O_3 has a high estimated critical electric field of $\sim$8 MV cm^{-1} (Refs. 2 and 3) and a decent electron mobility of $\sim$200 cm^2 V^{-1} s^{-1},[4–8] resulting in a high Baliga's figure of merit that outperforms that of conventional power semiconductors, such as SiC and GaN. Furthermore, the fabrication cost of β-Ga_2O_3 single crystals via melt growth[9–12] is lower than that of SiC and GaN bulk crystals grown from vapor phases. Because of these two advantages over the competing semiconductors, β-Ga_2O_3 has emerged as a next-generation power semiconductor, thereby attracting attention among semiconductor research communities. Although the unipolarity of β-Ga_2O_3 can be an obstacle for device applications, promising device prototypes, such as Schottky barrier diodes (SBDs),[13–17] metal-oxide-semiconductor field-effect transistors (MOSFETs),[18–22] and modulation-doped field-effect transistors (MODFETs),[23–27] have been demonstrated. Particularly, recently demonstrated fin FETs (FinFETs)[28–33] and trench MOS-type SBDs (MOSSBDs)[34–37] have exhibited excellent device performances, in which the fins and trenches aid in achieving normally off operation[28,29,31–33] and high reverse breakdown voltages,[34,36,37] respectively, by regulating the current flow in the confined regions without using p–n junctions.

Plasma-based anisotropic dry etching has been widely used to create such sophisticated device structures. Almost all β-Ga_2O_3 devices with fins/trenches reported to date have been fabricated using reactive ion etching (RIE) with chlorine-based chemistry, which is now virtually the de facto standard etching technique in the β-Ga_2O_3 community.[38] However, the RIE process causes plasma damage on the processed surfaces, resulting in interface traps that degrade device performances due to limited effective channel mobility[31] and a large hysteresis loop[28] in FinFETs and increased on-resistance in MOSSBDs.[35] To restore device performances, the plasma damage should be removed through wet treatments in acid or alkaline solutions,[39–42] annealing,[41,43] or self-reaction etching with gallium flux.[42]

However, plasma-free anisotropic etching approaches have been explored to produce plasma-damage-free high-aspect-ratio structures. So far, various etching techniques, such as hot phosphoric acid etching,[44,45] metal-assisted chemical etching (MacEtch),[46,47] atomic gallium flux etching in an ultra-high vacuum environment,[48] and hydrogen environment anisotropic thermal etching (HEATE),[49] have been reported, where the strong anisotropic nature of the β-Ga_2O_3 crystal structure is more or less reflected in the etched structures. In terms of MacEtch, damage-free multiple fin channels were produced, and nearly zero-hysteresis operation of the FinFET was demonstrated.[50] However, the practical application of MacEtch is difficult because of its complicated etching system, in which etching proceeds very slowly ($\sim$100 nm/h) in a hydrofluoric acid solution under deep-UV illumination using a patterned Pt layer as a catalytic mask.[46] Additionally, the sidewall profiles of the MacEtch-formed fins on (010) substrates are positively tapered even when the fins are designed along vertical cleavage planes such as (100), indicating its weak anisotropy.[47] In contrast, HEATE is the most promising method among all non-plasma-based etching methods in terms of simplicity and resulting etched profiles. HEATE is based on hydrogen-assisted thermal decomposition[51] and has recently been reported by Kikuchi *et al.* for SiO_2-masked (010) β-Ga_2O_3 substrates.[49] They investigated the in-plane anisotropic etching behavior to find that (100) and $\{10\bar{1}\}$ facets had the slowest and second-slowest lateral etching rates, respectively. Moreover, they succeeded in fabricating very high-aspect-ratio fins with (100)-faceted perfectly flat and vertical sidewalls without plasma damage that can be applied to distributed Bragg reflectors and nanofluidic channels. However, HEATE or the equivalent plasma-free dry etching method has not been applied to (001)-oriented β-Ga_2O_3 substrates, although most β-Ga_2O_3-based vertical power devices, including FinFETs and MOSSBDs, have now been fabricated on them.[15–17,22,31–37] Therefore, it is essential to investigate a plasma-free dry etching on (001) substrates to fabricate fins/trenches for vertically structured β-Ga_2O_3-based power devices.

In our previous study, we demonstrated selective area growth using HCl-based halide vapor phase epitaxy (HVPE) on (010) and (001) β-Ga_2O_3 substrates to fabricate plasma-damage-free fins/trenches as a bottom-up growth method.[52] In this growth system, the introduction of HCl etching gas in addition to the growth precursors was required for the suppression of parasitic gas-phase reaction and undesirable nucleation on the mask to achieve perfect selectivity. Furthermore, the excessive HCl gas supply led to selective area etching of the substrate in the window areas, which could be used as a plasma-free dry etching technique.

In this study, we investigated selective area HCl gas etching of (001) β-Ga_2O_3 substrates. Scanning electron microscopy (SEM) of the etched depressions revealed that the structures were dominated by (100) and {310} facets. In particular, (100) facets were smooth and free of plasma damage, although they were slightly inclined from the substrate normal. Therefore, gas-etched fins/trenches with faceted sidewalls can be applied to sophisticated power devices, including FinFETs and MOSSBDs.

We performed the HCl gas etching of β-Ga_2O_3 as follows. A circular-, radial-line-, stripe-, and square (100×100 μm^2)-patterned SiO_2 masks (0.1-μm thickness) were prepared on (001) β-Ga_2O_3 substrates. The masks were fabricated via conventional photolithography. The details of the process are found in our previous study.[52] The gas-phase etching was performed using a laboratory-made HCl-based HVPE system under atmospheric pressure. This system can directly supply a gas mixture of HCl (>99.999% pure) and N_2 (dew point $< -110\,^{\circ}C$) to the substrate.[53] In this study, an HCl/N_2 gas mixture with an HCl partial pressure of 63 Pa was supplied to the heated SiO_2-masked β-Ga_2O_3 substrate. Here, the substrate was vertically held at the center of the rotating holder in a horizontal quartz tube reactor, with the substrate surface perpendicular to the horizontal gas flow direction. Because the etching rate may strongly depend on the temperature, as verified in the H_2 etching experiments,[51] we first examined etching rates of the (001) surface at the different reactor temperatures of 521, 750, 863, and 1038 °C by measuring the depths in the square windows (100×100 μm^2) using a stylus profiler. The extracted etching rate monotonically increased with the temperature (Fig. S1), indicating that the rate can be controlled by the temperature. In this paper, we focused on the sample etched with the highest etching rate at 1038 °C and investigated its etching behaviors. We used SEM to characterize the etched structure's shape. Ga-focused ion milling was used to expose the cross section after depositing of a carbon surface protective layer. Atomic force microscopy was used to observe the surface morphology of the etched (001) surface.

The HCl gas etching of β-Ga_2O_3 proceeded not only in the window area but also under the mask. When the acceleration voltage (V_{acc}) is high enough to allow primary electrons to pass through the mask, the trace of the under-etching can be observed using SEM from the surface side without removing the mask. Figures 1(a) and 1(b) compare SEM images of the same circular pattern observed at different V_{acc}s of 1 and 10 kV. When $V_{acc} = 1$ kV, only a part of the etched region was visible through the circular window [Fig. 1(a)]. However, when $V_{acc} = 10$ kV, an etched region under the mask was observed [Fig. 1(b)]. This high-V_{acc} condition allowed us to observe the outline of the etched depression and the relative positional relationship between the window edge and depression simultaneously, allowing us to measure the under-etching length [Fig. 1(c)]. Thus, to understand the etching behaviors, including under-etching features, we did not remove the mask and set V_{acc} to 10 kV when observing the etched structures from the surface side. Note that the etched structures without the mask were also observed with SEM after removing the mask

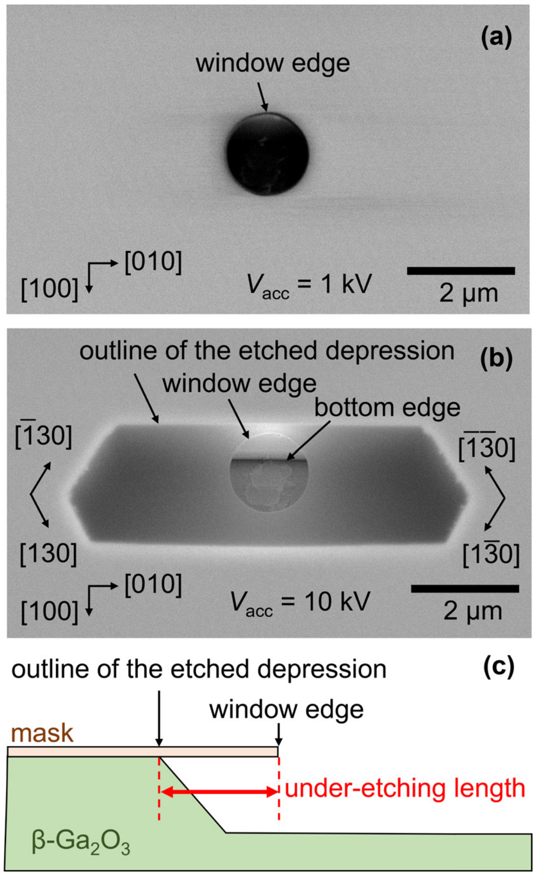

FIG. 1. Top-view scanning electron microscopy images of the etched trench on the same circular-patterned mask (1.7 μm in window diameter) recorded at (a) $V_{acc} = 1$ kV and (b) 10 kV. (c) Schematic cross section of the etched depression in the vicinity of the window edge, which illustrates the definition of under-etching length.

(Figs. S2–S5). Figure 1(b) also shows the in-plane anisotropic etching behavior. Although the window was circular, the surface edges of the etched depression were parallel to the crystallographic directions of [010], $[\bar{1}30]$, and [130] to form an elongated hexagon. This shape transformation from circular to elongated hexagon could be due to the monoclinic β-Ga_2O_3 crystal structure.[54]

We investigated the in-plane anisotropic etching behavior in more detail using two radial-line window patterns. The designs of the two patterns are as follows: For one pattern, window lines were placed every 10° (36 lines), one of which was along [010] [Fig. 2(a)]. For the other pattern, window lines were placed along crystallographic orientations parallel to possible oxygen sublattice planes (16 lines) [Fig. 2(b)]. Note that $[hk0]$ and $[\bar{h}\bar{k}0]$ are crystallographically equivalent. For these radial lines, under-etching lengths perpendicular to the window lines were measured using SEM and summarized in a polar plot [Fig. 2(c)]. The notation of $n_{[hk0]}$ indicates the direction rotated counterclockwise by 90° from $[hk0]$ on the substrate surface. Note that $n_{[hk0]}$ and $n_{[\bar{h}\bar{k}0]}$ are crystallographically equivalent.

The polar plot shows the in-plane orientation dependence of the under-etching length in detail. The under-etching was the fastest along the vicinity of $n_{[\bar{1}90]}$, $n_{[\bar{1}\bar{9}0]}$, and their equivalent directions to make the largest peaks in the plot. The second fastest orientation was [010]. However, under-etching was the slowest along $[\bar{1}00]$ and [100] to make sharp and deep dips because of the emergence of (100) facets that have the smallest surface energy density.[55] The under-etching was also suppressed along $n_{[\bar{1}30]}$, $n_{[\bar{1}\bar{3}0]}$, and their equivalent directions to form small dips, which is attributed to the formation of {310} facets that are slip planes, consisting of close-packing planes of the oxygen sublattice.[56] Generally, such planes with low surface-energy-density exhibit chemical resistance to form faceted structures during etching, which is consistent with our present results. Note that the polar plot of the under-etching length is not perfectly symmetric. There is a small but significant difference between the under-etching lengths of the upper half ($[\bar{1}00]$ side) and the lower half ([100] side) of the polar plot. For example, under-etching lengths along $[\bar{1}00]$ and [100] were ∼0.1 and ∼0.6 μm, respectively, although the corresponding $(\bar{1}00)$ and (100) facets are crystallographically equivalent and should have the same surface energy density. How the difference arose based on the results of cross-sectional SEM observation is described later.

We focused on the stripe arrays along [010] to further investigate the etched structures with (100) facets. We used two stripe patterns with different widths of mask/window (hereinafter patterns A and B). The widths of the mask/window were 2.8/1.2 μm for pattern A and 1.0/5.5 μm for pattern B. Under-etching should be minimized in a practical etching process to allow fine patterning. In this case, [010] is the most favorable window direction. Figure 3 shows top- and tilted-view SEM images of the trenches formed along [010] by the etching through the striped windows of pattern A [Figs. 3(a)–3(c)] and pattern B [Figs. 3(d)–3(f)]. In both cases, HCl etching formed trenches under the windows with small under-etching lengths of less than 0.7 μm. Furthermore, flat and smooth (100)-faceted sidewalls were observed on the $[\bar{1}00]$ side (see also Fig. S4). In addition to the (100)-faceted sidewalls, relatively rough and inclined facets appeared at the bottom corners of the [100] side, as indicated by the $(h0l)$ label in Fig. 3(f). This facet is discussed later. Moreover, in the case of pattern B, narrow fins with a width of approximately 0.3 μm were formed between the trenches because of the narrow mask width [Figs. 3(d)–3(f)],

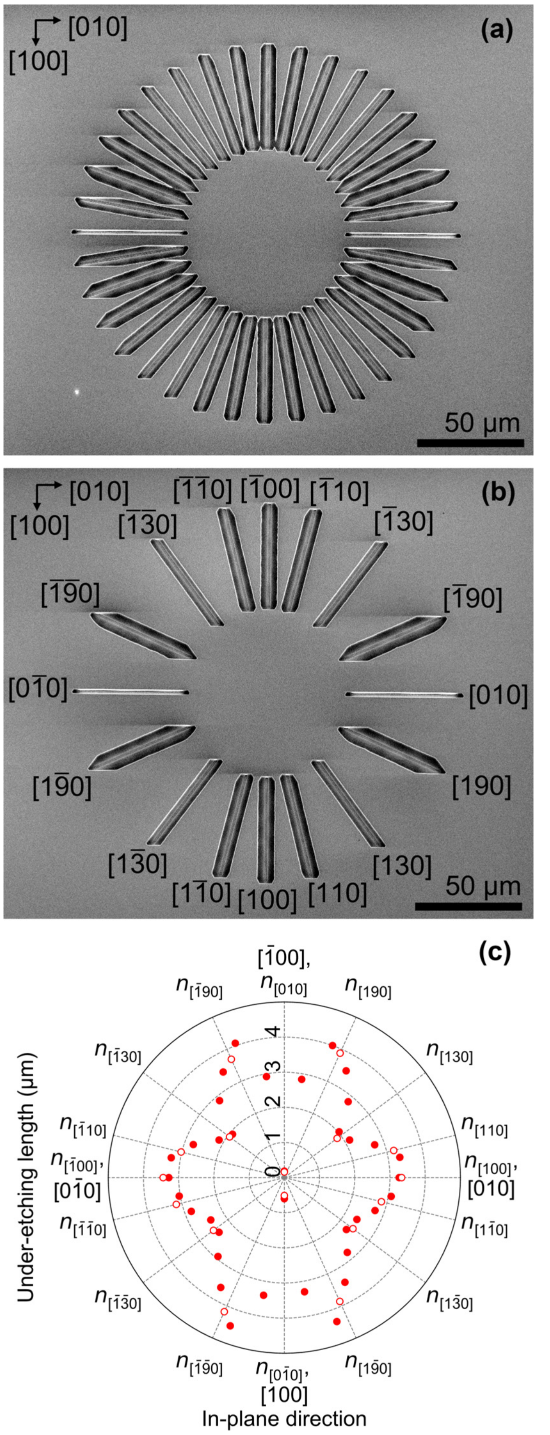

FIG. 2. Top-view scanning electron microscopy images of the etched trenches on the radial-line-patterned masks (1.2 μm in window width), where the lines were patterned (a) every 10° and (b) along crystallographic orientations parallel to the possible oxygen sublattice planes. (c) Polar plot of under-etching length measured from pattern (a) (filled circles) and pattern (b) (open circles). See the text about the notation of $n_{[hk0]}$.

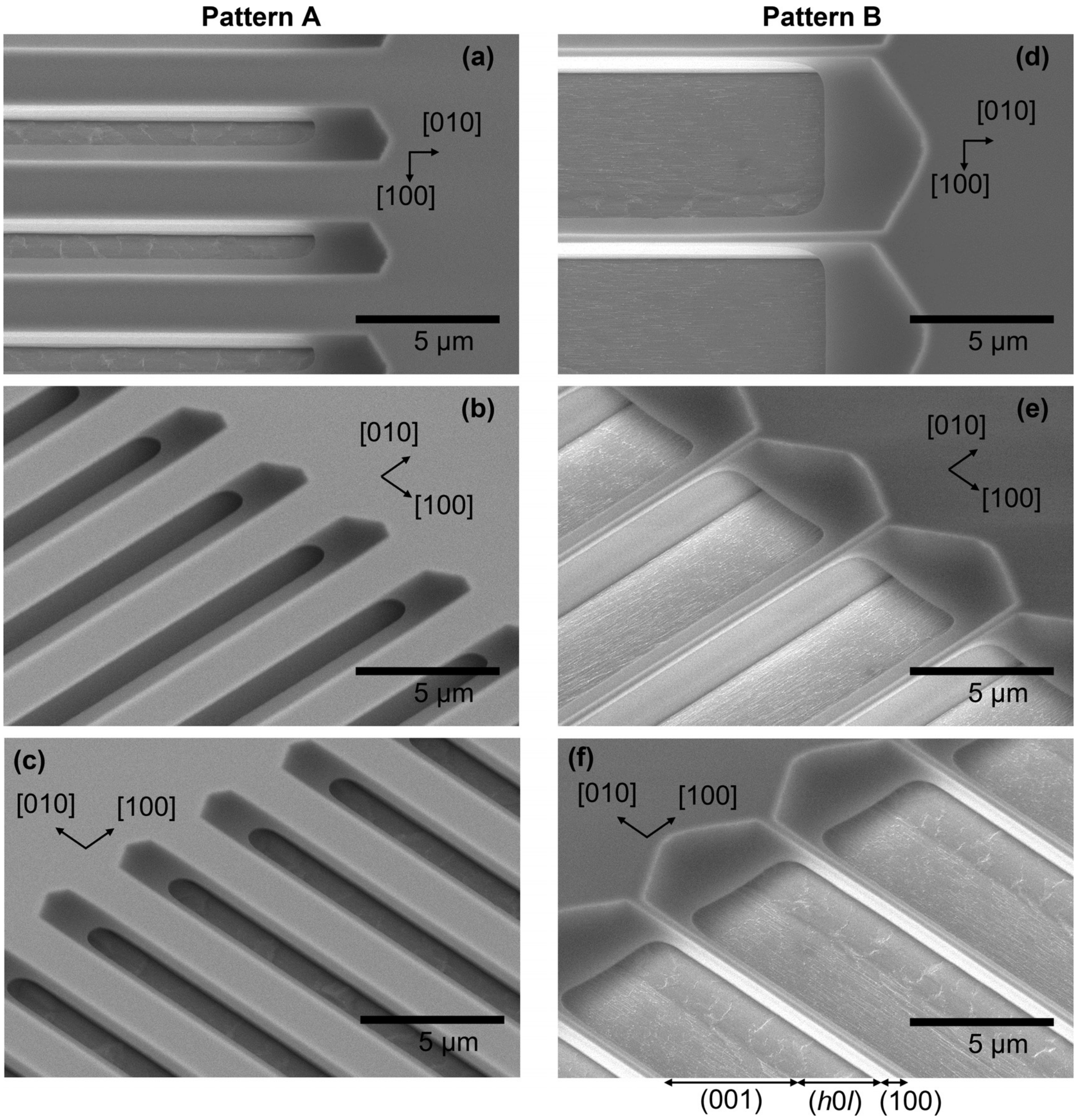

FIG. 3. Top- and tilted-view scanning electron microscopy images (0° and 50° from the surface normal, respectively) of etched trenches produced using the [010]-oriented stripe masks of (a)–(c) pattern A and (d)–(f) pattern B.

indicating that gas etching can fabricate not only trenches but also fins. Aside from these sidewalls, the surface morphology of the etched (001) bottom surface was measured using AFM, as shown in Fig. S6. The surface was relatively rough with the RMS roughness of 7.7 nm due to the presence of macro steps along [010] and byproducts deposited on the surface. Similar macro steps along [010] were observed for HVPE growth on (001) substrates,[52] and, thus, the suppression of the formation of these steps should be a tough challenge. However, the deposited byproducts could be removed by optimizing the etching conditions, which should be our future work.

Cross-sectional observation of the trenches along [010] revealed more detailed information about the etched structures with (100)-faceted sidewalls. SEM images of the cross-sectional structures of the trenches corresponding to patterns A and B are shown in Figs. 4(a) and 4(b), respectively. Schematic cross-sectional structures for both patterns are also shown in Fig. 4(c). Both sidewalls of the trenches have inclined (100) facets. The face angles between the (100) facets and surface (001) were measured to be 103°–105°, which agrees with the lattice angle $\beta = 103.7°$.[54] The inclination of the (100) facets could have caused uneven under-etching behavior between $[\bar{1}00]$ and [100]. The (100) facet should be formed almost immediately on the $[\bar{1}00]$ side because the plane was positively tapered. Therefore, the under-etching length on the $[\bar{1}00]$ side was very short because the etching rate was minimized soon after the (100) facet was formed. However, the negatively tapered (100) facet should take longer to form on the [100] side because more crystal volume must be removed. The etching

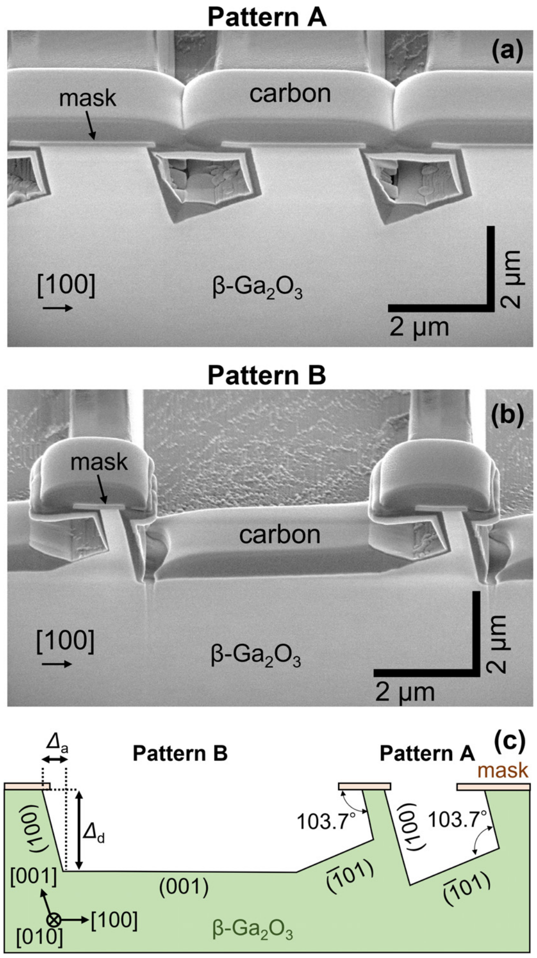

FIG. 4. (a) and (b) Tilted-view scanning electron microscopy images (54° from the surface normal) of cross-sectional structures of the trenches corresponding to Figs. 3(a)–3(c) (pattern A) and 3(d)–3(f) (pattern B). The carbon depositions near the cross sections are surface protective layers. Note that different scales should be used to measure vertical and lateral lengths on the cross sections. (c) Schematic cross sections for both patterns.

would proceed with planes other than (100) during the transitional period, and the etching rate should be faster than that of (100). Therefore, fast etching should occur for a longer time to increase the under-etching length on [100] side longer. The inclined planes at the bottom corners of the [100] side were identified as $(\bar{1}01)$ facets using cross-sectional SEM images. The measured face angles between the $(\bar{1}01)$ and the (100) facets were 100°–102°, whose measured values were close to the calculated face angle of 103.7°. The emergence of the $(\bar{1}01)$ facet agrees with the fact that $(\bar{1}01)$ exhibited the next slowest etching rate to (100) among the planes belonging to the [010] zone based on the HEATE method.[49] Interestingly, the trench bottom was solely formed by the $(\bar{1}01)$ facet when the window width was small (pattern A) [Fig. 4(a)].

Using the geometry described in Fig. 4(c), the etching depth (Δ_d) can be calculated using the following relationship:

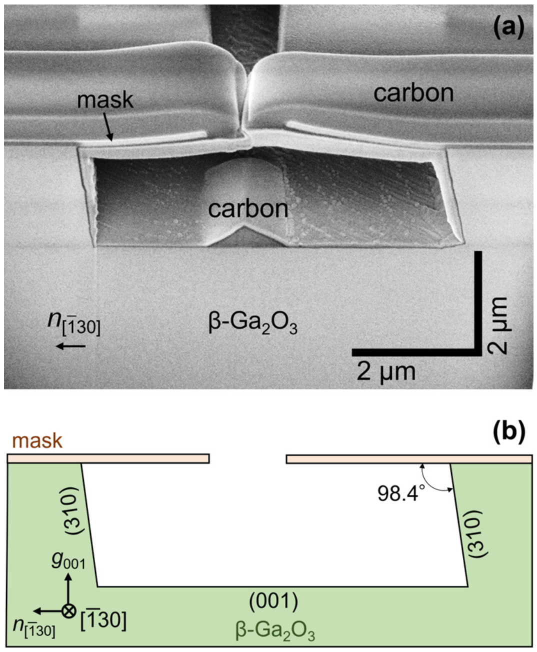

FIG. 5. (a) Tilted-view SEM images (54° from the surface normal) of a cross-sectional structure of the etched trench produced using the line-patterned mask (1.2 μm in window width) along $[\bar{1}30]$, which are one of the radial lines in Fig. 2(b). (b) Schematic cross section corresponding to (a).

$$\Delta_d = \cot(\beta - 90^\circ)\Delta_a \sim 4.1\Delta_a,$$

where Δ_a is the projected length of the inclined (100) facet on (001), which can be measured using top-view SEM. For instance, Δ_a is measured to be 0.47 μm from the top-view SEM image for the narrow window pattern A [Fig. 3(a)], and Δ_d is extracted to be 1.9 μm. This value agrees with the observed depth of $\Delta_d = 1.8\,\mu$m obtained from the corresponding cross-sectional SEM image [Fig. 4(a)]. Given that such narrow trenches cannot be probed with a stylus or cantilever, the depth estimation method described above is very useful.

We also characterized the cross-sectional structure of an etched trench with {310}-faceted sidewalls. As discussed above, {310} facets had the second slowest lateral etching rate for forming faceted trench sidewalls. Thus, the cross-sectional structure of the trench with {310}-faceted sidewalls is worth investigating. Figure 5(a) shows a cross-sectional SEM image of the trench formed by the etching through a line-shaped window along $[\bar{1}30]$, which is one of the radial lines shown in Fig. 2(b). A schematic of the cross section is shown in Fig. 5(b). The trench profile was defined solely by inclined (310)-faceted sidewalls and a (001)-faceted bottom. The cross-sectional profile is simpler than that of the [010]-oriented trench made using the pattern B, which has (100)-faceted sidewalls and an additional $(\bar{1}01)$ facet at the bottom corner (compare Figs. 4 and 5). The measured face angles of the (310) facets from the surface were 98°–99°, which were very close to the calculated angle of 98.4°. However, the (310) sidewalls were relatively rough due to the presence of macro steps, as evidenced by the SEM image recorded after removing the mask (Fig. S5). The generation of macro steps could be caused by the emergence of (100) facets. Therefore, the (310) faceted sidewalls are unfavorable for practical fin/trench applications.

In conclusion, we used plasma-free HCl gas etching on a (001) β-Ga_2O_3 substrate to investigate its potential as a fin/trench fabrication process. After systematic characterization of the etched structures, we concluded that the direction of stripe windows should be along [010] to fabricate fins and trenches with faceted sidewalls of (100). Although (100) facets are inclined from the substrate's normal by 13.7°, their smooth and plasma-damage-free sidewall surfaces can improve the performances of fin/trench devices on (001) substrates. We consider such facet-formation-based fin/trench fabrication methods by plasma-free dry etching, and our previously proposed selective area growth will contribute to the development of the fabrication process of β-Ga_2O_3 devices.

See the supplementary material for the etching rate of (001) surface as a function of reactor temperature (Fig. S1), etched structures after removing the SiO_2 mask (Figs. S2–S5), and surface morphology of the etched (001) surface characterized by AFM (Fig. S6).

The preparation of the SiO_2 patterned mask and the characterization of the etched structures were performed at the Namiki Foundry and the Nanofabrication Facility (Project No. 22 NM5110) in the National Institute for Materials Science.

AUTHOR DECLARATIONS

Conflict of Interest

The authors have no conflicts to disclose.

Author Contributions

Takayoshi Oshima: Conceptualization (equal); Methodology (equal); Writing – original draft (lead). **Yuichi Oshima:** Conceptualization (equal); Methodology (equal); Writing – review & editing (lead).

DATA AVAILABILITY

The data that support the findings of this study are available from the corresponding author upon reasonable request.

REFERENCES

[1] A. J. Green, J. Speck, G. Xing, P. Moens, F. Allerstam, K. Gumaelius, T. Neyer, A. Arias-Purdue, V. Mehrotra, A. Kuramata, K. Sasaki, S. Watanabe, K. Koshi, J. Blevins, O. Bierwagen, S. Krishnamoorthy, K. Leedy, A. R. Arehart, A. T. Neal, S. Mou, S. A. Ringel, A. Kumar, A. Sharma, K. Ghosh, U. Singisetti, W. Li, K. Chabak, K. Liddy, A. Islam, S. Rajan, S. Graham, S. Choi, Z. Cheng, and M. Higashiwaki, APL Mater. **10**, 029201 (2022).

[2] J. L. Hudgins, G. S. Simin, E. Santi, and M. A. Khan, IEEE Trans. Power Electron. **18**, 907 (2003).

[3] M. Higashiwaki, K. Sasaki, A. Kuramata, T. Masui, and S. Yamakoshi, Appl. Phys. Lett. **100**, 013504 (2012).

[4] N. Ma, N. Tanen, A. Verma, Z. Guo, T. Luo, H. (Grace) Xing, and D. Jena, Appl. Phys. Lett. **109**, 212101 (2016).

[5] Z. Feng, A. F. M. Anhar Uddin Bhuiyan, M. R. Karim, and H. Zhao, Appl. Phys. Lett. **114**, 250601 (2019).

[6] Y. Zhang, F. Alema, A. Mauze, O. S. Koksaldi, R. Miller, A. Osinsky, and J. S. Speck, APL Mater. **7**, 022506 (2019).

[7] L. Meng, Z. Feng, A. F. M. A. U. Bhuiyan, and H. Zhao, Cryst. Growth Des. **22**, 3896 (2022).

[8] Z. Feng, A. F. M. A. U. Bhuiyan, Z. Xia, W. Moore, Z. Chen, J. F. McGlone, D. R. Daughton, A. R. Arehart, S. A. Ringel, S. Rajan, and H. Zhao, Phys. Status Solidi RRL **14**, 2000145 (2020).

[9] E. G. Víllora, K. Shimamura, Y. Yoshikawa, K. Aoki, and N. Ichinose, J. Cryst. Growth **270**, 420 (2004).

[10] A. Kuramata, K. Koshi, S. Watanabe, Y. Yamaoka, T. Masui, and S. Yamakoshi, Jpn. J. Appl. Phys., Part 1 **55**, 1202A2 (2016).

[11] Z. Galazka, J. Appl. Phys. **131**, 031103 (2022).

[12] E. Ohba, T. Kobayashi, T. Taishi, and K. Hoshikawa, J. Cryst. Growth **556**, 125990 (2021).

[13] T. Oshima, T. Okuno, N. Arai, N. Suzuki, S. Ohira, and S. Fujita, Appl. Phys. Express **1**, 011202 (2008).

[14] K. Sasaki, A. Kuramata, T. Masui, E. G. Víllora, K. Shimamura, and S. Yamakoshi, Appl. Phys. Express **5**, 035502 (2012).

[15] K. Konishi, K. Goto, H. Murakami, Y. Kumagai, A. Kuramata, S. Yamakoshi, and M. Higashiwaki, Appl. Phys. Lett. **110**, 103506 (2017).

[16] C.-H. Lin, Y. Yuda, M. H. Wong, M. Sato, N. Takekawa, K. Konishi, T. Watahiki, M. Yamamuka, H. Murakami, Y. Kumagai, and M. Higashiwaki, IEEE Electron Device Lett. **40**, 1487 (2019).

[17] P. Dong, J. Zhang, Q. Yan, Z. Liu, P. Ma, H. Zhou, and Y. Hao, IEEE Electron Device Lett. **43**, 765 (2022).

[18] M. Higashiwaki, K. Sasaki, T. Kamimura, M. Hoi Wong, D. Krishnamurthy, A. Kuramata, T. Masui, and S. Yamakoshi, Appl. Phys. Lett. **103**, 123511 (2013).

[19] M. H. Wong, K. Sasaki, A. Kuramata, S. Yamakoshi, and M. Higashiwaki, IEEE Electron Device Lett. **37**, 212 (2016).

[20] A. J. Green, K. D. Chabak, M. Baldini, N. Moser, R. Gilbert, R. C. Fitch, G. Wagner, Z. Galazka, J. Mccandless, A. Crespo, K. Leedy, and G. H. Jessen, IEEE Electron Device Lett. **38**, 790 (2017).

[21] M. H. Wong, Y. Nakata, A. Kuramata, S. Yamakoshi, and M. Higashiwaki, Appl. Phys. Express **10**, 041101 (2017).

[22] K. Zeng, R. Soman, Z. Bian, S. Jeong, and S. Chowdhury, IEEE Electron Device Lett. **43**, 1527 (2022).

[23] T. Oshima, Y. Kato, N. Kawano, A. Kuramata, S. Yamakoshi, S. Fujita, T. Oishi, and M. Kasu, Appl. Phys. Express **10**, 035701 (2017).

[24] E. Ahmadi, O. S. Koksaldi, X. Zheng, T. Mates, Y. Oshima, U. K. Mishra, and J. S. Speck, Appl. Phys. Express **10**, 071101 (2017).

[25] S. Krishnamoorthy, Z. Xia, C. Joishi, Y. Zhang, J. McGlone, J. Johnson, M. Brenner, A. R. Arehart, J. Hwang, S. Lodha, and S. Rajan, Appl. Phys. Lett. **111**, 023502 (2017).

[26] C. Joishi, Y. Zhang, Z. Xia, W. Sun, A. R. Arehart, S. Ringel, S. Lodha, and S. Rajan, IEEE Electron Device Lett. **40**, 1241 (2019).

[27] A. Vaidya, C. N. Saha, and U. Singisetti, IEEE Electron Device Lett. **42**, 1444 (2021).

[28] K. D. Chabak, N. Moser, A. J. Green, D. E. Walker, S. E. Tetlak, E. Heller, A. Crespo, R. Fitch, J. P. McCandless, K. Leedy, M. Baldini, G. Wagner, Z. Galazka, X. Li, and G. Jessen, Appl. Phys. Lett. **109**, 213501 (2016).

[29] Y. Zhang, A. Mauze, F. Alema, A. Osinsky, T. Itoh, and J. S. Speck, Jpn. J. Appl. Phys., Part 1 **60**, 014001 (2021).

[30] Z. Hu, K. Nomoto, W. Li, L. J. Zhang, J.-H. Shin, N. Tanen, T. Nakamura, D. Jena, and H. G. Xing, in *75th Annual Device Research Conference* (IEEE, 2017).

[31] Z. Hu, K. Nomoto, W. Li, Z. Zhang, N. Tanen, Q. T. Thieu, K. Sasaki, A. Kuramata, T. Nakamura, D. Jena, and H. G. Xing, Appl. Phys. Lett. **113**, 122103 (2018).

[32] Z. Hu, K. Nomoto, W. Li, N. Tanen, K. Sasaki, A. Kuramata, T. Nakamura, D. Jena, and H. G. Xing, IEEE Electron Device Lett. **39**, 869 (2018).

[33] W. Li, K. Nomoto, Z. Hu, T. Nakamura, D. Jena, and H. G. Xing, in *IEEE International Electron Devices Meeting* (IEEE, 2019), pp. 12.4.1–12.4.4.

[34] K. Sasaki, D. Wakimoto, Q. T. Thieu, Y. Koishikawa, A. Kuramata, M. Higashiwaki, and S. Yamakoshi, IEEE Electron Device Lett. **38**, 783 (2017).

[35] W. Li, K. Nomoto, Z. Hu, D. Jena, and H. G. Xing, IEEE Trans. Electron Devices **68**, 2420 (2021).

[36] W. Li, K. Nomoto, Z. Hu, D. Jena, and H. G. Xing, IEEE Electron Device Lett. **41**, 107 (2020).

[37] F. Otsuka, H. Miyamoto, A. Takatsuka, S. Kunori, K. Sasaki, and A. Kuramata, Appl. Phys. Express **15**, 016501 (2022).

[38] R. Khanna, K. Bevlin, D. Geerpuram, J. Yang, F. Ren, and S. Pearton, *Gallium Oxide* (Elsevier, 2019), pp. 263–285.

[39] Y. Zhang, A. Mauze, F. Alema, A. Osinsky, and J. S. Speck, Appl. Phys. Express **12**, 044005 (2019).

[40] H.-K. Lee, H.-J. Yun, K.-H. Shim, H.-G. Park, T.-H. Jang, S.-N. Lee, and C.-J. Choi, Appl. Surf. Sci. **506**, 144673 (2020).

[41] Z. Wang, X. Yu, H. Gong, T. Hu, Y. Zhang, X. Ji, F. Ren, S. Gu, Y. Zheng, R. Zhang, A. Y. Kuznetsov, and J. Ye, J. Phys. Chem. Lett. **13**, 7094 (2022).

[42] B. Feng, T. He, G. He, X. Zhang, Y. Wu, X. Chen, Z. Li, X. Zhang, Z. Jia, G. Niu, Q. Guo, Z. Zeng, and S. Ding, Appl. Phys. Lett. **118**, 181602 (2021).

[43] J. Yang, F. Ren, R. Khanna, K. Bevlin, D. Geerpuram, L.-C. Tung, J. Lin, H. Jiang, J. Lee, E. Flitsiyan, L. Chernyak, S. J. Pearton, and A. Kuramata, J. Vac. Sci. Technol., B **35**, 051201 (2017).

[44] T. Oshima, T. Okuno, N. Arai, Y. Kobayashi, and S. Fujita, Jpn. J. Appl. Phys., Part 1 **48**, 040208 (2009).

[45] Y. Zhang, A. Mauze, and J. S. Speck, Appl. Phys. Lett. **115**, 013501 (2019).

[46] M. Kim, H.-C. Huang, J. D. Kim, K. D. Chabak, A. R. K. Kalapala, W. Zhou, and X. Li, Appl. Phys. Lett. **113**, 222104 (2018).

[47] H. Huang, M. Kim, X. Zhan, K. Chabak, J. D. Kim, A. Kvit, D. Liu, Z. Ma, J.-M. Zuo, and X. Li, ACS Nano **13**, 8784 (2019).

[48] N. K. Kalarickal, A. Fiedler, S. Dhara, H.-L. Huang, A. Bhuiyan, M. W. Rahman, T. Kim, Z. Xia, Z. J. Eddine, A. Dheenan, M. Brenner, H. Zhao, J. Hwang, and S. Rajan, Appl. Phys. Lett. **119**, 123503 (2021).

[49] Y. Yamazaki, M. Tomoaki, A. Takeki, and A. Kikuchi, in 4th International Workshop on Gallium Oxide and Related Materials, 2022.

[50] H.-C. Huang, Z. Ren, A. F. M. Anhar Uddin Bhuiyan, Z. Feng, Z. Yang, X. Luo, A. Q. Huang, A. Green, K. Chabak, H. Zhao, and X. Li, Appl. Phys. Lett. **121**, 052102 (2022).

[51] R. Togashi, K. Nomura, C. Eguchi, T. Fukizawa, K. Goto, Q. T. Thieu, H. Murakami, Y. Kumagai, A. Kuramata, S. Yamakoshi, B. Monemar, and A. Koukitu, Jpn. J. Appl. Phys., Part 1 **54**, 041102 (2015).

[52] T. Oshima and Y. Oshima, Appl. Phys. Express **15**, 075503 (2022).

[53] Y. Oshima, S. Yagyu, and T. Shinohe, J. Cryst. Growth **576**, 126387 (2021).

[54] S. Geller, J. Chem. Phys. **33**, 676 (1960).

[55] S. Mu, M. Wang, H. Peelaers, and C. G. Van de Walle, APL Mater. **8**, 091105 (2020).

[56] H. Yamaguchi, A. Kuramata, and T. Masui, Superlattices Microstruct. **99**, 99–103 (2016).